Hindawi
Geofluids
Volume 2022, Article ID 9948658, 15 pages
https://doi.org/10.1155/2022/9948658

Research Article

Influence of Drying–Wetting Cycles on the Water Retention and Microstructure of Residual Soil

Xu-tang Xu,[1] **Dao-qi Liu**,[1] **Zhen-xing Xian**,[1] **Feng Yang**,[1] **Wen-bin Jian**,[2] **Xiang Xu**,[1] **and Jian-bin Huang**[1]

[1]*College of Transportation and Civil Engineering, Fujian Agriculture and Forestry University, No. 63 Xiyuangong Road, University Town, Fuzhou 350108, China*
[2]*College of Environment and Resources, Fuzhou University, No. 2 Xueyuan Road, University Town, Fuzhou 350116, China*

Correspondence should be addressed to Xu-tang Xu; xxtmdd@163.com

Received 30 May 2022; Revised 21 July 2022; Accepted 2 August 2022; Published 30 August 2022

Academic Editor: Xianwei Zhang

Due to frequent changes in the humid and hot environment, the residual soil with a particle-size distribution (PSD) from gravel to clay experiences multiple drying–wetting cycles. The pressure plate test and nuclear magnetic resonance (NMR) spectroscopy were used to investigate the influence of drying–wetting cycles on the soil–water characteristic curve (SWCC) and pore-size distribution (POSD) of undisturbed residual soil. The results showed that the water-holding capacity of the residual soil decreased as the number of drying–wetting cycles increased and gradually stablilized, and then the van Genuchten (VG) model was found to perform well on the SWCC during the drying–wetting processes. The NMR results indicated a double-pore structure, and the porosity of the residual soil as well as the internal water content increased smoothly with more drying–wetting cycles. The obtained POSD curve of soil implied that drying–wetting cycles had a more obvious effect on small pores and macro-pores than on micro-pores and meso-pores. Theoretical calculations evinced that the product of the matric suction and relaxation time should be constant at a constant temperature. However, the experimental results did not effectively reflect such a relation between the matric suction and relaxation time. A modified VG model based on the cumulative pore volume was utilized to describe the POSD under drying–wetting cycles. Subsequently, the proposed Rational2D surface equation was used to accurately reflect the internal relationship between the SWCC and POSD curve under different numbers of drying–wetting cycles. Moreover, the fractal model for the SWCC derived from the capillary theory confirmed that the matric suction had a strong linear relationship with the relative volumetric water content in the log-log scale. Also, the fractal dimension can be approximated as a constant, because its attenuation is small with more drying–wetting cycles.

1. Introduction

Residual soils are widely distributed in the world, whose weathering degree of the parent rock is closely related to the hot and humid climate. Hence, a thick layer of residual soil commonly forms in the subtropical and tropical marine climates [1]. The seasonal climatic variability, namely, the drying–wetting cycle, causes significant changes to the residual soil's physicochemical properties, such as the fabric, particle cementation characteristic, water content, and porosity. These structural changes to the residual soil seriously affect the engineering performance of the rock and soil mass [2, 3]. The microstructure and formation of micro-cracks increase the compressibility and hydraulic conductivity of the soil, reducing its structural strength and stability. Therefore, research on the evolution of the micro-pore structure and water-holding capacity of residual soil in drying–wetting environments is important for ensuring the stability of slopes and for preventing and controlling landslide disasters.

The soil–water characteristic curve (SWCC) describes the relationship between the water content (or saturation) and matric suction, and the mechanical properties of soil, such as permeability, strength, and deformation, are closely related to the water-holding curve [4–6]. Most experimental methods for determining the soil SWCC are based on

porous clay plates and axis translation, including the tensiometers, pressure plate technique, filter paper method, and thermal conductivity sensors. Nevertheless, all of these methods are laborious, so numerous studies predicted the SWCC using other indirect approaches. Currently, methods for predicting the SWCC can be mainly divided into three categories: the first category is established the correlation relationship connecting fitting parameters in the SWCC equations with soil basic characteristics (Table 1 summarizes four representative equations of this method in the literature); the second category is to establish the statistical correlation between matric suction and water content based upon the regression analysis of functional parameters [7–9]; the third category is to use a physical empirical model constructed from the pore-size distribution (POSD) curve for estimation [10–14].

In consideration of the cumulative POSD curve of the soil is similar to the SWCC in shape, it is more acceptable to use the POSD curve to predict the SWCC. Due to different pore structures in soil samples, a typical SWCC can be either unimodal or bimodal [19]. For well-graded soils, the internal POSD and SWCC usually show a unimodal characteristic, that is, a continuous *S*-shaped curve. However, soils with dual porosity structure (such as residual and colluvial soils) composed of macro-pores (inter-agglomerate pores) and micro-pores (intra-agglomerate pores) are usually associated with the POSD and SWCC showing a bimodal characteristics (i.e., it contains two continuous *S*-shaped curves). Although the traditional unimodal SWCC equation cannot be directly used to describe the bimodal SWCC, the continuous bimodal SWCC equation can be considered the superposition of two unimodal SWCC equations. The common practice is to modify the classical unimodal SWCC model (i.e., the four formulas given in Table 1) to predict the bimodal SWCC [13, 20, 21].

The fractal theory has become an important method in microscopic analysis of unsaturated soils due to its simple thinking, few parameters, and strong effectiveness [22]. The structures of the soil, such as surface characteristics and pore distribution characteristics, can be represented by fractal models [23]. Soldi et al. [24] proposed a constitutive model of unsaturated soils based on the fractal theory. Tao et al. [25] established a SWCC prediction model considering fractal characteristics of pores based on the fractal theory. Jin et al. [26] proposed a fractal SWCC model of soil in the full suction range, which can reflect the film flow in the high suction section under dry conditions. The internal pore structure and POSD of the soil are sensitive to the drying–wetting history, which in turn affects the shape of the SWCC. Previous studies have shown that the internal structure and POSD of the soil are most affected by the first drying–wetting cycle and that the soil structure gradual stabilizes with further drying–wetting cycles [27–30]. Seeing that the range of the POSD directly reflects the permeability and water-holding capacity of the soil, several approaches are developed to quantify the soil POSD from porous materials, including mercury intrusion porosimetry (MIP), the water vapor or nitrogen adsorption method, X-ray computed tomography (CT), and scanning electron microscopy (SEM). However, these methods are limited in applicability and test conditions [31–33]. For example, MIP often needs to use high pressure to measure the small pores of the structure, but this can easily fracture cementation bonds and fragment grains, degrading the accuracy of the measurement results. The nitrogen adsorption method can only measure the distribution of small pores of soil. CT and SEM are imaging technologies, and they are time-consuming to restore the pore structure distribution inside the soil with the help of a large quantity of image information. Obviously, the above methods are not applicable to this prespecified study due to the tested soil is low-density residual soil with particle-size distributions from gravel to clay; similar descriptions were also obtained by Kong et al. [34], Pires et al. [35], Wang et al. [36] and Wen et al. [33].

Nuclear magnetic resonance (NMR) spectroscopy was developed in the mid-1940s, and it takes advantage of the physical interaction between low-energy electromagnetic waves (i.e., radio waves) and matter. Since NMR technology can overcome abovementioned shortcomings, it is gradually applied in the field of geotechnical engineering from the medical, chemical, and industrial fields to evaluate soil moisture migration, porosity, and POSD [36–40]. Numerous researchers have studied the water-holding capacity, strength and deformation characteristics, permeability–strength characteristics, and crack evolution law of soil under drying–wetting cycles. At the same time, the relationship between the macro-mechanical characteristics and microstructural characteristics of expansive soil [41–43], unsaturated sand [44], sliding zone soil [45, 46], compacted loess [47–50], and clay soil [51–53] was evaluated to reveal the intrinsic nature of soil strength attenuation at the microscale. We can also conclude that most of the previous investigations on the SWCC under multiple drying–wetting cycles have focused on slope stability analysis or pollutant migration. However, the effect of multiple drying–wetting cycles on the SWCCs of undisturbed residual soil, especially the applicability of three typical SWCC models, the internal relationship between the SWCC and POSD and fractal dimension *D*, is still far from being clearly understood and need further discussion. In this study, undisturbed residual soil from Fujian Province was used to study the relationship between the water-holding capacity, internal microstructure, and POSD under multiple drying–wetting cycles. A pressure plate test and NMR spectroscopy were used to evaluate the evolution of the soil microstructure under periodic drying–wetting cycles and its relationship with the SWCC. Such studies will be expected to serve as a reference for evaluating possible changes in the microstructure of residual soil that undergoes periodic drying and wetting processes.

2. Material and Methods

2.1. Illustrative Descriptions of Soil Specimens. Soil samples were taken from Fuzhou City in Fujian Province at a depth of 3 m. The soil was reddish brown. X-ray diffraction showed that the soil comprised quartz, feldspar, kaolinite, montmorillonite, palygorskite, and other minerals. Table 2 presents the basic physical properties of the residual soil, and the

Table 1: Typical SWCC equations for the first category of methods from the literature.

Refs	Equations	Notations
Brooks-Corey model [15]	$\Theta = \frac{\theta - \theta_r}{\theta_s - \theta_r} = \begin{cases} 1 \cdots \text{for} \cdots \psi \le \psi_e \\ \left[\frac{\psi_e}{\psi}\right]^{\lambda} \cdots \psi > \psi_e \end{cases}$	where θ is volumetric water content; θ_s is saturated volumetric water content; θ_s is residual volumetric water content; Θ is normalized water content; ψ_e is air entry value or air expulsion value of soil; ψ is the matric suction; λ is pore size distribution index.
Gardner model [16]	$\theta = \theta_r + \frac{\theta_s - \theta_r}{1 + a\psi^b}$	Where a is soil parameters related to the air entry value or air expulsion value of soil; b is the soil parameters connected with the water outflow (or water inflow) in the soil when the matric suction exceeds the air entry value (or air expulsion value).
Van Genuchten model [17]	$\theta = \theta_r + \frac{\theta_s - \theta_r}{[1 + (\alpha\psi)^n]^m}$	Where α is soil parameters related to the inverse of the air entry value or air expulsion value of soil; n is the fitting parameters connected with the pore size distribution of the soil; m is fitting parameter allied to the asymmetry of the model, and m=1-1/n.
Fredlund-Xing model [18]	$\theta = \left[1 - \frac{\ln(1 + (\psi/\psi_r))}{\ln\left(1 + \left(10^6/\psi_r\right)\right)}\right] \frac{\theta_s}{\left\{\ln\left[e + (\psi/a)^b\right]\right\}^c}$	Where a is soil parameters related to the air entry value or air expulsion value of soil; b is the soil parameters connected with the water extraction (or water insert) rate in the soil when the matric suction exceeds the air entry value (or air expulsion value); c is the soil parameters allied to the rate of residual water content; ψ_r is the matric suction in residual state; $C(\psi)$ is the correction factor corresponding to residual matric suction.

Table 2: Physical and mechanical properties of residual soil.

Specific gravity G_s	Water content w (%)	Void ratio e	Liquid limit w_L (%)	Plastic limit w_p (%)	Particle-size characteristics of the residual soil/%			
					Fine gravel >2 mm	Sand 0.075~2 mm	Silt 0.005~0.075 mm	Clay <0.005 mm
2.68	26.5	1.06	45	26	3.7	30.3	39.6	25.4

dry density (ρ_d) of the residual soil is 1.3 g/cm^3, which is a low-density soil. Figure 1 shows the cumulative PSD curve of the residual soil, which contained 3.7% gravel, 30.3% sand, 39.6% silt, and 25.4% clay.

2.2. Testing Procedure Using the Pressure Plate Extractor and NMR System. The geo-expert stress-related SWCC pressure plate instrument system was used to obtain the SWCC of the soil samples, by dint of the MesoMR23-060H-I NMR analysis and imaging system, the obtained NMR signal was subjected to inversion to get the T_2 spectrum and porosity of the soil at different drying–wetting cycles, then the NMR imaging results were used to generate a cross-sectional pseudo-color image of the saturated soil samples.

The water content of natural soil varies considerably at shallow depths. Field surveys showed that the residual soil had a minimum mass water content as low as about 17% and a maximum mass water content close to saturation. Therefore, the change in water content during the drying–wetting cycle test was controlled between 17% and saturation. To determine the SWCC of the residual soil, undisturbed residual soil with a water content of about 17% was pressurized by vacuum saturation to 1000 kPa and was then drained. The air pressure was then gradually reduced, and the soil sample gradually absorbed water. This comprised a drying–wetting cycle. The above steps were repeated until the target number of cycles (one, two, three, five, and seven) was completed. The main steps of the SWCC test were reported by Xu and Jian [54]. Data were recorded every 12 h throughout the test. The suction balance standard was as follows: the volume of the sample absorbed or discharged within 24 h did not exceed 0.05% of the soil sample volume.

For the NMR test, the saturated sample was first dried in an oven at 40°C for 72 h. The water content was measured every 2 h until the sample reached 15%. The sample was then cooled to room temperature of 25°C. Vacuum saturation was performed for 48 h, which completed a drying–wetting cycle. This was repeated for a predetermined number of cycles (two, three, five, and seven). Considering the NMR test is nondestructive and repeatable, both the drying–wetting cycles and NMR tests were performed on one sample.

3. Analysis and Results

3.1. Analysis of the Soil–Water Characteristic Curve (SWCC). To better analyze and compare the applicability of different SWCC equations, it is useful to reflect the evolution of limited experimental data points over the full suction range in the form of a continuity equation. Due to the discontinuity of the Brooks-Corey equation in the near-saturated state, it cannot effectively predict the water-holding capacity of the soil, and many fitting parameters can provide stronger prediction correlations. The three-parameter Gardner model and Van Genuchten (VG) model and the four-parameter VG model and the Fredlund-Xing (FX) model were used to fit the SWCC curves of the residual soil under different

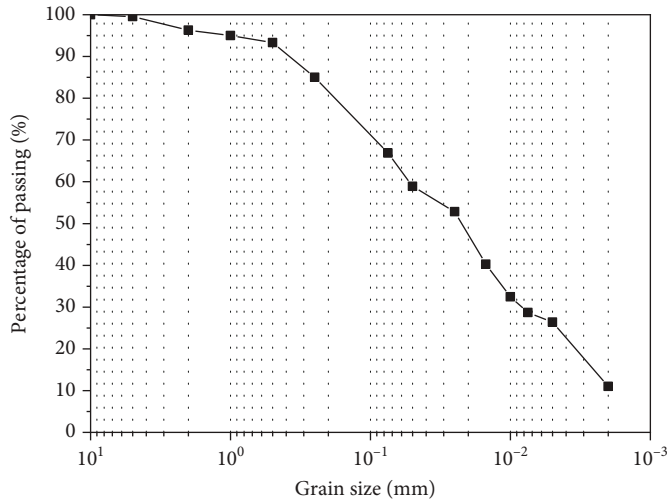

Figure 1: Cumulative curve of soil particle-size distribution.

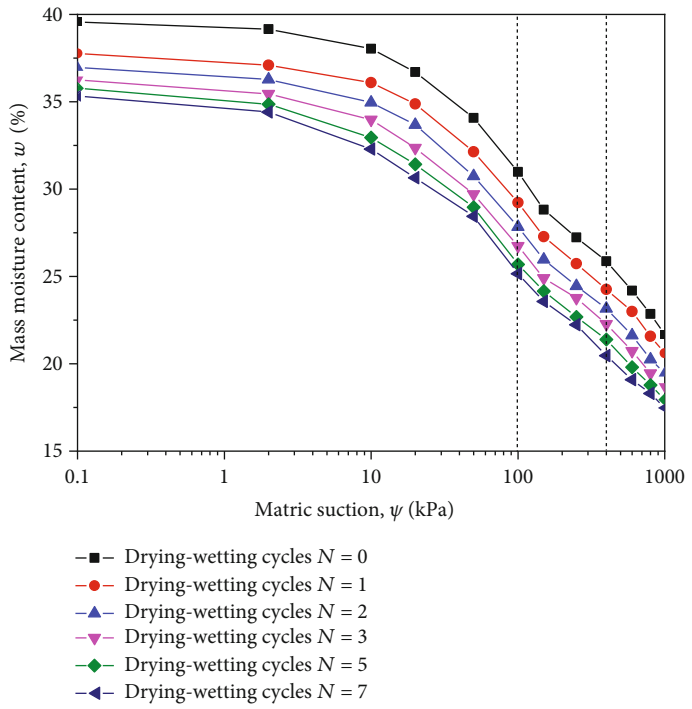

Figure 2: SWCC of residual soil under different drying–wetting cycle conditions.

numbers of drying–wetting cycles obtained from the pressure plate test. By assuming that there is a certain causal relationship between the matric suction and saturation, the correlation coefficient $R^2(\theta)$ is used as a quantitative index to characterize the fitting effect. The closer the correlation coefficient is to 1, the smaller the error between the water content calculated by different SWCC equations and the measured value is. Figure 2 shows the variation in the mass water content of the residual soil with the matric suction under different numbers of drying–wetting cycles. When the number of drying–wetting cycles was 0, 1, 2, 3, 5, and 7, the saturated volumetric water content of the soil was 0.5148, 0.4913, 0.4808, 0.4716, 0.4653, and 0.4596, respectively. The SWCCs and best-fitting parameters of the undisturbed residual soil obtained by using the nonlinear equation in drying–wetting cycles are presented in Tables 3 and 4 and Figures 3 and 4. On the whole, the correlation coefficients of the four models were all greater than 0.9955, implying that the three-parameter or four-parameter equations match well with the calculated data of the residual soil. It should also be noted that the three-parameter VG model is better than the Gardner model, while the four-parameter FX model has slightly better fitting performance than the VG model. Combined with the fitting effect and the simplicity of the formula,

Table 3: Best-fit parameters and R^2 values for the Gardner and VG model (three-parameter).

Drying–wetting cycles N	θ_s	Three-parameter equations							
		Fitting parameters of Gardner model				Fitting parameters of VG model; $m = 1 - 1/n$			
		θ_r	a	b	R^2	θ_r	α	n	R^2
0	0.5148	0.2551	0.0109	0.9204	0.9955	0.1122	0.0361	1.2311	0.9964
1	0.4913	0.2393	0.0137	0.8787	0.9958	0.0840	0.0426	1.2045	0.9966
2	0.4808	0.2231	0.0161	0.8592	0.9968	0.0616	0.0493	1.1961	0.9972
3	0.4716	0.2104	0.0216	0.8092	0.9972	0.0556	0.0646	1.1871	0.9973
5	0.4653	0.1917	0.0279	0.7632	0.9980	0.0471	0.0749	1.1822	0.9980
7	0.4596	0.1898	0.0305	0.7518	0.9990	0.0315	0.0834	1.1736	0.9992

Table 4: Best-fit parameters and R^2 values for the VG and FX model (four-parameter).

Drying–wetting cycles N	θ_s	Four-parameter equations									
		Fitting parameters of VG model; m is free					Fitting parameters of FX model				
		θ_r	α	n	m	R^2	ψ_r	α	n	m	R^2
0	0.5148	0.1171	0.0354	1.2233	0.1934	0.9964	70378.4	35.2289	1.0711	0.4413	0.9964
1	0.4913	0.1092	0.0382	1.1635	0.1992	0.9967	94590.7	32.7317	1.0175	0.4561	0.9966
2	0.4808	0.1039	0.0398	1.1097	0.2199	0.9974	99779.1	30.4296	0.9853	0.4914	0.9974
3	0.4716	0.1028	0.0434	1.0312	0.2412	0.9977	101301.1	26.3695	0.9339	0.5122	0.9977
5	0.4653	0.1016	0.0437	0.9396	0.2767	0.9984	111086.9	24.9481	0.8585	0.5635	0.9985
7	0.4596	0.1006	0.0463	0.9274	0.2853	0.9995	123237.1	24.3699	0.8302	0.5928	0.9996

the four-parameter VG model can be preferentially used to simulate the SWCC of the undisturbed residual soil under different numbers of drying–wetting cycles.

The initial saturated volumetric water content and residual volumetric water content decreased as the number of drying–wetting cycles increased; in other words, the water-holding capacity decreased. This was caused by the destruction of the internal bonding structure of the soil and increase in pore volume during the drying–wetting cycles. This can also be related to crack propagation. During dehumidification, the water in the soil flowed out of the large and small pores successively, which caused the soil to gradually shrink and crack [55, 56]. While in the process of humidification, the water first entered the small pores and then entered the macro-pores. Hydrolysis reduced the initial and solidified cohesion between particles, and the loss of fine particles in the soil and the expansion of clay particles during water migration further aggravated the development of the initial cracks in the soil [52, 57, 58]. The internal microstructure of the soil was irreversibly deformed by the repeated changes in the suction path. The micro-cracks in the soil propagated and expanded, which gradually formed a water transport channel. The number of meso-pores and macro-pores in the soil gradually increased; this decreased the water absorption rate of the soil during the wetting part of the cycle, which lowered the saturation point [46, 59].

Table 2 implies that the first drying–wetting cycle had an obvious effect on the SWCC. According to the fitting parameters of the VG model, both α and m increased with more drying–wetting cycles, while n gradually decreased. The air expulsion value (AExV) at zero, one, two, three, five, and seven drying–wetting cycles were 28.3, 26.2, 25.1, 23.0, 22.9, and 21.6 kPa, respectively. Thus, the AExVs decreased as the number of drying–wetting cycles increased. At more than five drying–wetting cycles, n increased to an average value of 1.1319. At fewer than five drying–wetting cycles, n decreased to an average value of 0.9335. This shows that more drying–wetting cycles increased the range of the pore-size distribution inside the soil. The parameter m reflects the degree of curvature of the transition curve from the SWCC boundary zone to the transition zone. At more than five drying–wetting cycles, m decreased to an average value of 0.2134. At more than five drying–wetting cycles (i.e., $N = 7$), m was relatively large with an average value of 0.2810. A larger m means a steeper curve and a smaller negative pressure corresponding to the same water content; similar results of fitting parameters change with the drying–wetting cycles can be obtained in other models. It is worth noting that increasing the number of drying–wetting cycles shifted the SWCC to the left, and a stable state was reached after five drying–wetting cycles. At this time, the internal structure of the soil tended to stabilize.

3.2. Microstructure Analysis. The NMR test results were used to analyze the effect of the number of drying–wetting cycles on the SWCC of the residual soil at the microscale. The transverse relaxation time T_2 spectrum, POSD, and magnetic resonance imaging (MRI) of the soil samples during the drying–wetting cycles were evaluated.

3.2.1. T_2 Spectral Distribution. Figure 5 shows the T_2 spectral distribution curves of the residual soil at different numbers of drying–wetting cycles. The abscissa and ordinate represent the transverse relaxation time T_2 and NMR signal

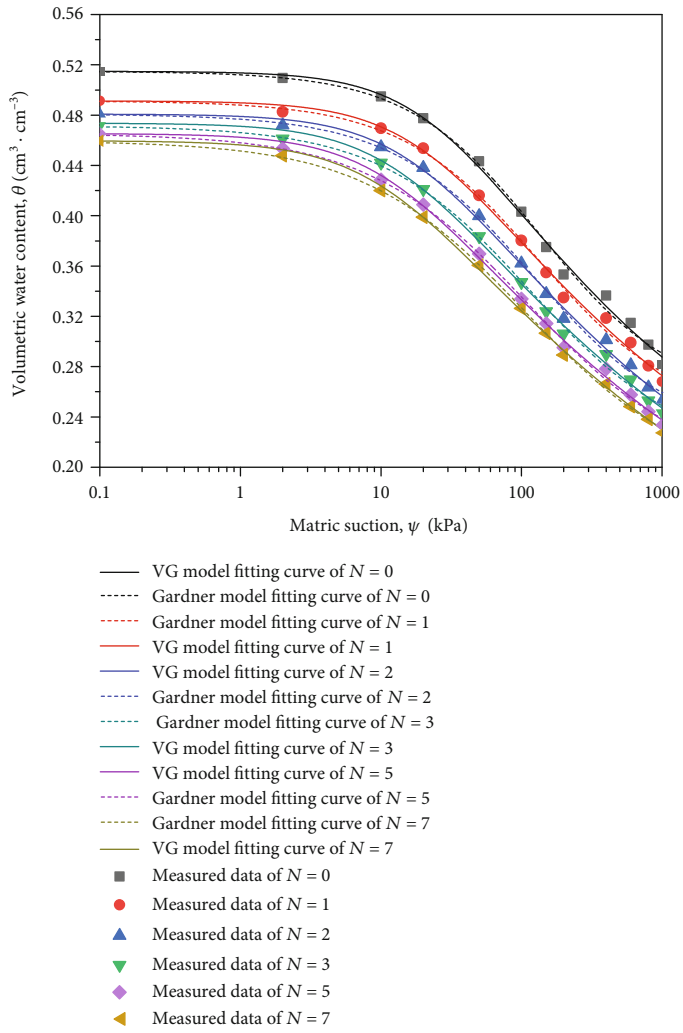

Figure 3: SWCC trend diagram of residual soil simulated by Gardner and VG model (three-parameter).

amplitude (dimensionless), respectively. At a zero drying–wetting cycle, two peaks in the T_2 spectrum had the minimum values, and the distribution interval was the smallest. Increasing the number of drying–wetting cycles tended to move the spectrum to the right and increased the values of both the primary and secondary peaks. At zero, one, two, three, five, and seven cycles, the main/secondary peaks of the soil mass had values of 390/18, 426/26, 449/36, 471/44, 496/48, and 515/55, respectively. The total area of the T_2 spectrum increased with an increase in the number of drying–wetting cycles N (11383, 12539, 13481, 14560, 15673, and 16389, respectively). The area of the T_2 spectrum reached a maximum value of 16389 during the seventh cycle.

The T_2 spectral distribution curve of the cohesive residual soil exhibited the same trend at different numbers of drying–wetting cycles with an obvious bimodal structure, indicating that the soil had a double-pore structure. The main peak was on the left with a short relaxation time but high signal amplitude, representing the microscopic pores inside the aggregate. The secondary peak was on the right with a long relaxation time but considerably lower signal amplitude, indicating the presence of macroscopic voids between aggregates. The bimodal POSD included pores between aggregates and the pores formed by particles connecting within aggregates. The pores between aggregates were relatively unstable, and they were easily affected by water immersion, pressure, and the number of drying–wetting cycles. However, the connections between the internal particles were relatively stable, and changes to the internal structure lagged behind the external conditions. The above analysis shows that the SWCC measured using the soil with bimodal POSD should present two sections: one with descending slopes and the other with a transition zone.

3.2.2. Pore-Size Distribution (POSD). The relaxation time T_2 of pore water in the soil is related to the pore structure as follows:

$$\frac{1}{T_2} = \rho_2 \frac{S}{V}, \tag{1}$$

where ρ_2 is the transverse relaxation rate and S/V is the ratio of the pore surface area to fluid volume ($S/V = \alpha/r$ where r is the pore radius and α is the pore shape factor).

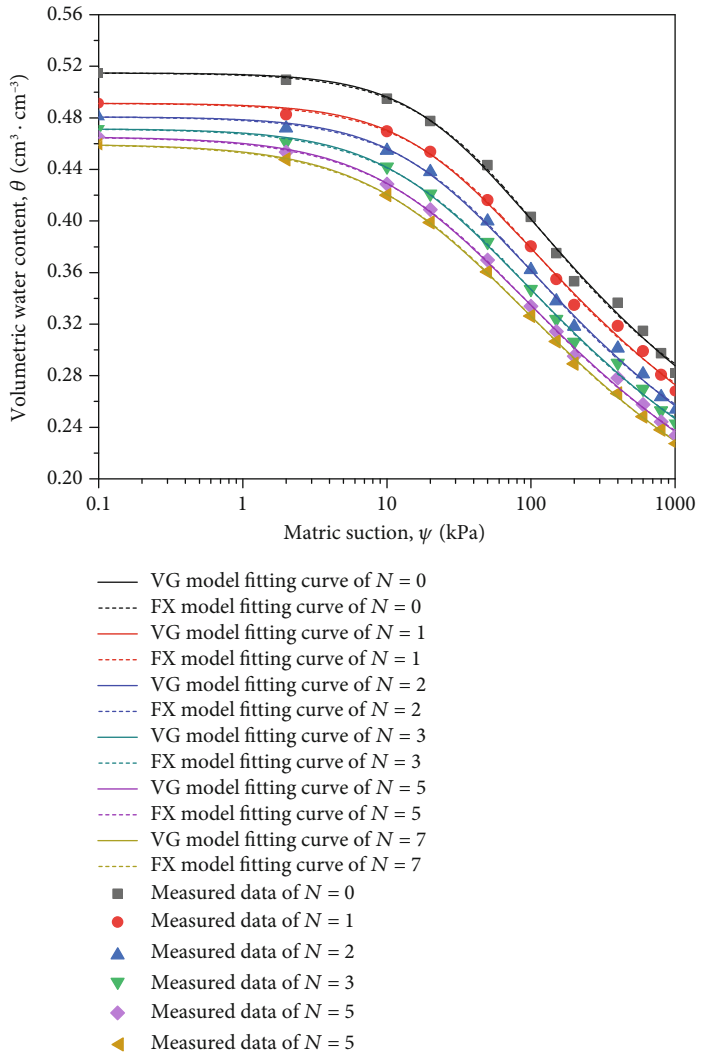

Figure 4: SWCC trend diagram of residual soil simulated by VG and FX model (four-parameter).

When the pores in the soil have a cylindrical shape, Equation ((1)) can be rewritten as

$$\frac{1}{T_2} = \rho_2 \frac{2}{r}. \tag{2}$$

Equation (2) shows that T_2 is proportional to the pore radius. Figure 6 shows the distribution of internal pores in the soil after drying–wetting cycles. Based on the test results and literature [21, 29, 34, 55, 56], the pores were divided into four categories according to the pore radius r. Micro-pores ($r < 1\,\mu m$) were present within particles. Small pores ($1\,\mu m \le r \le 2.5\,\mu m$) were pores between particles. Meso-pores ($2.5\,\mu m < r \le 10\,\mu m$) were pores in the aggregates. Macro-pores ($r > 10\,\mu m$) were pores between aggregates.

Figure 6 indicates that the soil in the natural state mainly comprised small pores and meso-pores (35% and 39%, respectively), followed by micro-pores (22%), and macro-pores (4%). With more drying–wetting cycles, the internal pores of the soil changed dynamically. The proportion of micro-pores and small pores decreased, while the proportion of meso-pores and macro-pores increased. In the first three drying–wetting cycles, the micro-pores and meso-pores decreased by 3.6% and 3.7%, respectively, on average and decreased by a maximum of 6.5% and 5.2%, respectively, during the second cycle. Meanwhile, the macro-pores increased by 36.3% on average and increased by 42.2% after the first cycle. In the fifth cycle, the micro-pores and small pores decreased by 0.3% and 4.8%, respectively, compared with the third cycle, while the meso-pores and macro-pores increased by 2.1% and 7.7%, respectively. In the final and seventh cycle, the micro-pores and micro-pores decreased by 1.1% and 0.9%, respectively, while the meso-pores and macro-pores increased slightly by 0.8% and 1.5%, respectively. These results demonstrate that the number of drying–wetting cycles had a more obvious effect on the small pores and macro-pores than on the micro-pores and meso-pores.

During the hygroscopic process, the internal pores and cracks of the soil were gradually filled with water. The increased water content promoted the dissolution of soluble minerals and cementitious materials, which weakened the

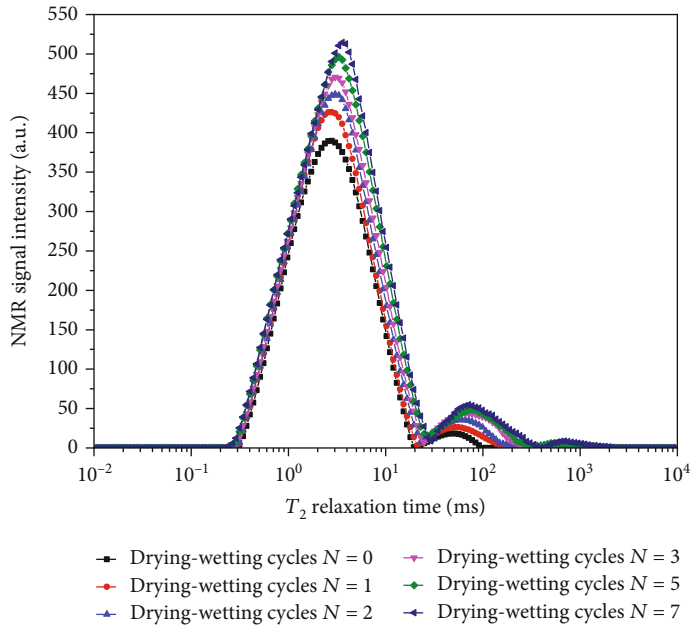

Figure 5: T_2 spectrum distribution curve of residual soil under different drying–wetting cycles.

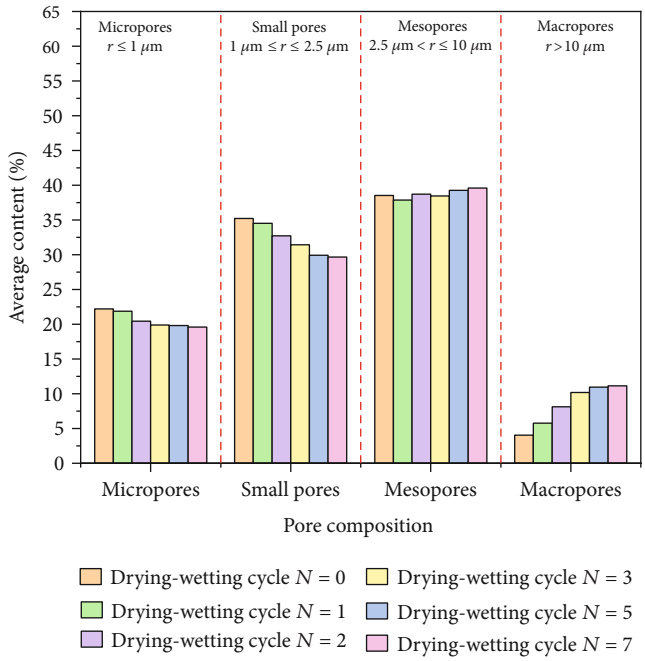

Figure 6: Distribution of various pore contents of samples under different drying–wetting cycles.

connection between soil particles. At the same time, the expansion pressure of the clay minerals increased due to water absorption, which led to cement fracture. Because of electrostatic attraction on the surface of the clay particles, polar water molecules were easily adsorbed during the wetting part of the cycle. This increased the thickness of the water film bonded to the soil particles, and thus, the pressure of water film wedging decreased the molecular attraction by increasing the distance between particles, resulting in the dispersion of aggregates into sub-aggregates. During the process of dehumidification, the drying kinetics caused water molecules to escape. This strengthened the connection between aggregates, and some sub-aggregates recombined, causing the expansion of shrunk micro-cracks and further water loss inside the soil. Regardless of whether the clay mineral particles expanded with water or shrank without water, irreversible deformation and failure would occur within and between the clay particles and aggregates, and new cracks would be derived. With more drying–wetting cycles, the micro-cracks in the soil further developed and connected (see Figure 7), which eventually led to the destruction of the soil microstructure.

The drying–wetting cycles caused the clay minerals in the soil to expand and contract as the microscopic pore water migrated back and forth. The fatigue damage caused by the changing internal microstructure of the soil manifested with the hydrolysis of cement particles, coarsening of pores, and crack formation [56, 59]. Meanwhile, the connection between aggregates was continuously destroyed, causing the dispersion of aggregates, coarsening of the original pores, formation of voids, and transformation of smaller pores into larger pores. Then, the connections between soil particles and aggregates were also destroyed, transforming the original closed pores (mainly micro-pores and small pores) into open pores. This caused the pores to connect and coarsen into large first-order pores (meso-pores or macro-pores). The tensile stress generated by uneven expansion and contraction resulted in the formation of new cracks (micro-pores), indicating that the number of micro-pores stayed constant with more drying–wetting cycles, while the proportion of small pores decreased and the proportions of meso-pores and macro-pores increased (see Figure 5). The alternating drying and wetting steps increased the number and volume of internal pores in the soil, which increased

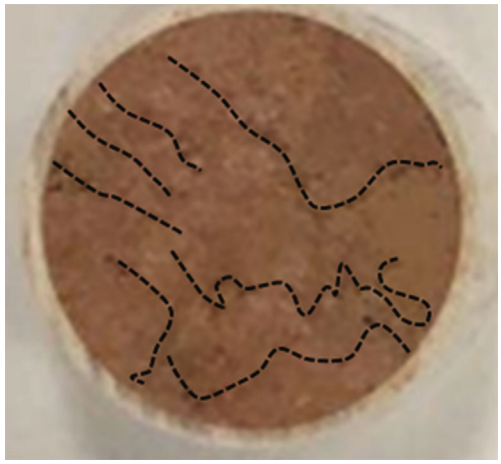

Figure 7: Cracks development photo of specimen after seven drying–wetting cycles.

the porosity. After zero, one, two, three, five, and seven drying–wetting cycles, the porosity changed to 51.5%, 54.2%, 57.6%, 59.1%, 61.5%, and 62.6%, respectively. The above analysis further shows that increasing porosity accelerated the channels in the soil to gradually connect and facilitated water migration. Consequently, the increasing range of the spectral area porosity gradually decreased.

3.2.3. MRI Analysis. Figure 8 shows MRI results of the residual soil at different numbers of drying–wetting cycles. The dark blue part in the pseudo-color map represents the background, and the bright area represents the location of water molecules and indicates the water content in the rock and soil. Thus, higher brightness revealed a greater water content and larger pores. The pore-water signal is uneven (see Figure 8), indicating that the structure of the cohesive residual soil had obvious heterogeneity and anisotropy. At the zero cycle, several bright areas can be observed in the middle of the image. This indicates a strong pore-water signal, and the soil mainly contained small pores and meso-pores. After three cycles, the soil pore structure changed significantly; the light-colored area in the lower right corner and middle part expanded, and the water signal increased. After seven cycles, the light-colored areas in the lower and middle of the image gradually expanded and connected. The bottom-left light-colored area formed an upside-down crescent. The above-mentioned phenomena well indicate that the water signal gradually increased and the soil porosity continuously connected as the number of drying–wetting cycle increased. In consequence, the original pore structure changed to form larger pores and the cracks expanded. Figure 8 directly represents the evolution of the internal pores of the soil during the drying–wetting cycles, and the change in the water signal is generally consistent with the T_2 spectral distribution curve, spectral area, and porosity of the residual soil.

4. Discussion

4.1. Derivation of the Empirical Equation. According to the Young–Laplace theory, the relationship between the matric suction ψ and effective pore radius r can be expressed as follows:

$$\psi = \frac{2T_s \cos \alpha}{r}, \tag{3}$$

where T_s is the surface tension and α is the contact angle between the water–air interface and solid phase. The relationship between the relaxation time and matric suction can be obtained by combining Equations (1) and (2):

$$\psi = \frac{T_s \cos \alpha}{\rho_2 T_2}, \tag{4}$$

where $T_s \cos \alpha / \rho_2$ is a constant under the condition of a constant temperature of 25°C. Theoretically, this means that the product of the matric suction and relaxation time should be a constant. Figure 9 shows the relationship between the cumulative pore-water mass per unit volume of soil and the relaxation time. The test data presented in Figure 2 were used to calculate the corresponding soil mass water content at different matric suctions according to Equation (1) and the fitting parameters presented in Table 4. The results were used with Equation (4) to evaluate whether the product of the matric suction and relaxation time (ψT_2) was constant at a constant temperature. The results showed that ψT_2 was not a fixed value for the residual soil. At $T_2 = 0$–9 ms, ψT_2 gradually decreased. At $T_2 = 9$–90 ms, ψT_2 gradually increased. At $T_2 > 90$ ms, ψT_2 gradually decreased. Overall, ψT_2 fluctuated considerably. This shows that the theoretical variation law of ψT_2 is difficult to describe owing to the influence of the drying–wetting cycles and different pore sizes.

4.2. Modified VG Model in Terms of Cumulative Pore Volume. The VG model reflects the relationship between the internal water content of the soil and the matric suction. The water content only reflects the overall amount of water, and it cannot reflect the detailed distribution characteristics of the pore water (i.e., the POSD). Therefore, the VG model and POSD curve for different numbers of drying–wetting cycles can be used to replace the matric suction with the pore radius to describe the change law of the cumulative pore volume per unit mass of soil. Then, the POSD law of soil under drying–wetting cycles is as follows:

$$V_r = V_0 + \frac{V_s - V_0}{\left[1 + (ar)^{-b}\right]^c}, \tag{5}$$

where V_r is the cumulative volume of pores (cm^3/g) smaller than the pore radius r and V_s and V_0 are the residual pore volume (cm^3/g) and saturated cumulative pore volume (cm^3/g), respectively. In addition, a, b, and c are empirical constants related to the solid phase characteristics of the soil. Equation (1) reflects the ratio of pore water to pore volume, while Equation (5) describes the pore-water distribution for different pore sizes. Figure 10 shows the relationship between the cumulative pore volume and pore radius, which

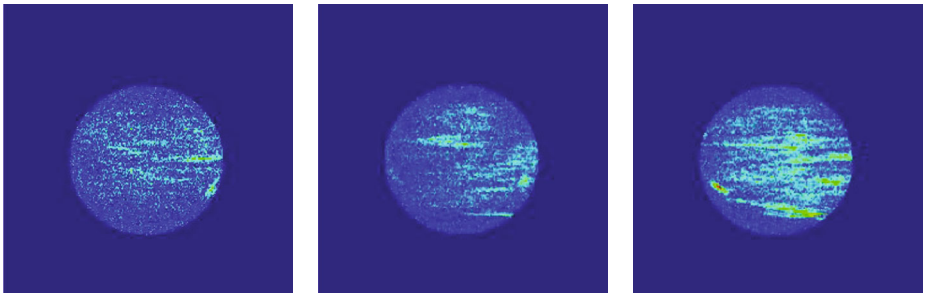

(a) N =1 (b) N =3 (c) N =7

Figure 8: NMR images of residual soil under different drying–wetting cycles.

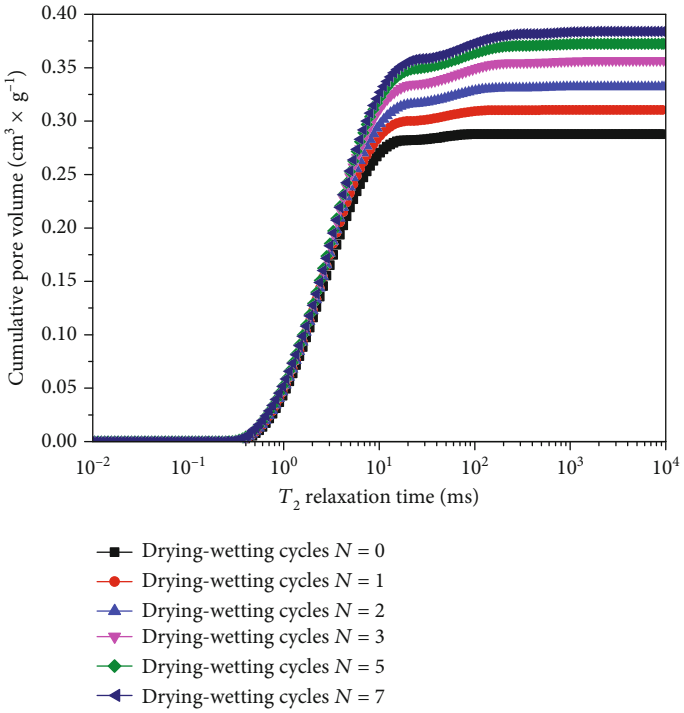

Figure 9: Relationships between cumulative pore volume and T_2 relaxation time.

has a typical S-shaped distribution. Therefore, the residual pore volume V_0 can be set to zero, and Equation (5) can be corrected as follows:

$$V_r = \frac{V_s}{\left[1 + (ar)^{-b}\right]^c}. \tag{6}$$

Table 5 presents the fitting results of the soil POSD at different numbers of drying–wetting cycles. The coefficient of determination R^2 was used to judge the goodness of fit. The fitting results showed that R^2 was greater than 0.999, representing a good fit. The POSD curve of the soil is closely related to the SWCC, which reflects the distribution characteristics of pores in the soil to some extent. Therefore, the fitting parameters of the SWCC and POSD curve have similar physical meanings. The fitting parameter a (Table 5) for the POSD curve describes the threshold pore size at the inflection point of the curve, which is inversely proportional to the AExV. The shape and variation trend of the SWCC and POSD curve are very similar. Therefore, the fitting parameters in Tables 4 and 5 can be used to establish a relationship between the SWCC and POSD curve under different numbers of drying–wetting cycles. Figure 11 shows the relationship between the SWCC and POSD curve corresponding to fitting parameters under different numbers of drying–wetting cycles. The surface comprises three curves: the number of drying–wetting cycles N in relation to the parameters α and a, N in relation to the parameters n and b, and N in relation to the parameters m and c. It can be seen from the fitting effect of Figure 11 that the surface satisfies the Rational2D function, and the specific equation is as follows:

$$z = \frac{z_0 + A_1 x + B_1 y + B_2 y^2 + B_3 y^3}{1 + A_2 x + A_3 x^2 + A_4 x^3 + B_4 y + B_5 y^2}, \tag{7}$$

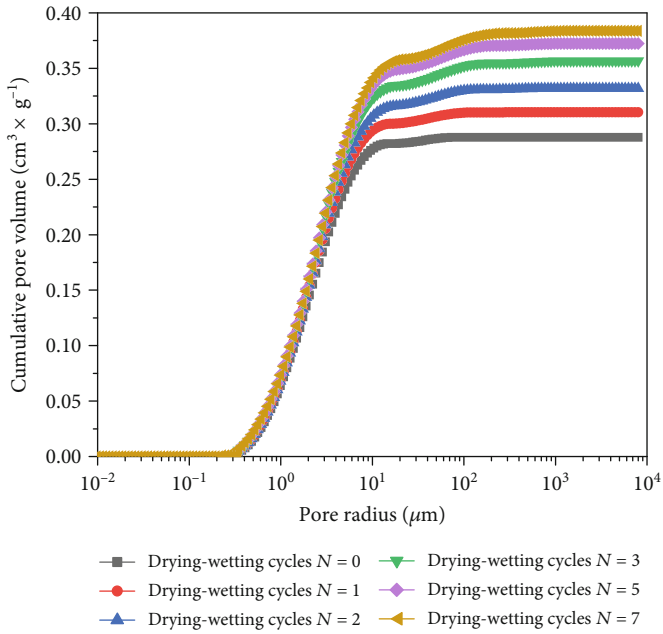

Figure 10: Relationships between cumulative pore volume and pore radius.

Table 5: Pore-size distribution fitting parameters of drying–wetting cycle samples.

Drying–wetting cycles N	V_s	a	b	c	R^2
0	0.2858	0.6037	1.7245	1.2835	0.9998
1	0.3103	0.6979	1.5783	1.5389	
2	0.3319	0.8176	1.4233	1.9199	
3	0.3569	0.9651	1.2659	2.2256	
5	0.3725	1.0161	1.2513	2.4131	
7	0.3838	1.0403	1.2105	2.5208	

where the z-axis is the parameter a (or b or c), the y-axis is the parameter α (or n or m), and the x-axis is the number of drying–wetting cycles N. Table 5 presents the fitting results of the surface equation, and $R^2 = 0.9958$. This demonstrates that the Rational2D function accurately reflects the internal relationship between the SWCC and POSD curve at different drying–wetting cycles. Although the SWCC is influenced by various factors, Figure 11 and Table 5 indicate that the SWCC of residual soil is significantly affected by the soil POSD at different drying–wetting cycles. The NMR test results showed that the T_2 relaxation method, which is a quick and simple way to determine the POSD, can be combined with Equation (7) to predict the water-holding capacity of residual soil at different drying–wetting cycles.

Table 6 presents the fitting results of the surface equation, and $R^2 = 0.9902$. This demonstrates that the Rational2D function accurately reflects the internal relationship between the SWCC and POSD curve under different numbers of drying–wetting cycles. Although the SWCC is influenced by various factors, Figure 11 and Table 6 indicate that the SWCC of residual soil is significantly affected by the soil POSD under different numbers of drying–wetting cycles.

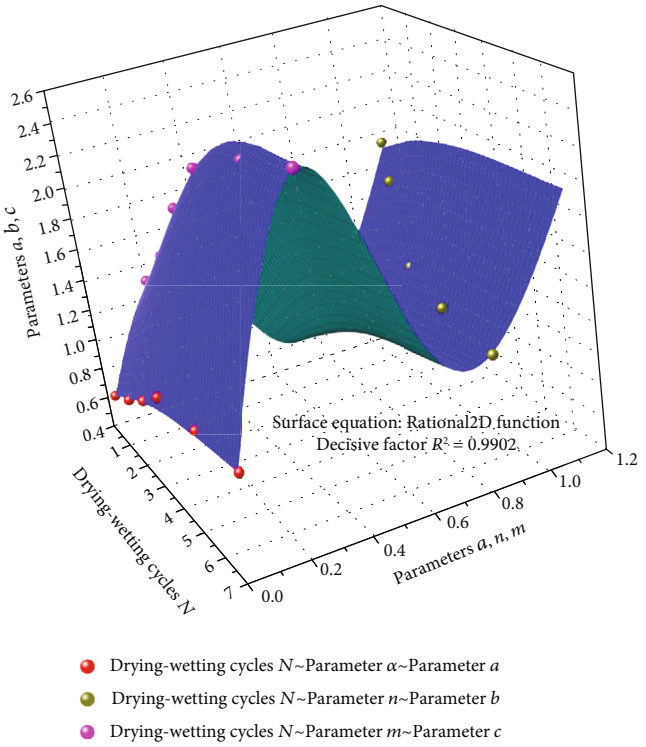

Figure 11: Relationship between SWCC curve parameters and POSD parameters under different drying–wetting cycles.

The NMR test results showed that the T_2 relaxation method, which is a quick and simple way to determine the POSD, can be combined with Equation (7) to predict the water-holding capacity of residual soil under different numbers of drying–wetting cycles.

Table 6: Fitting results of Rational2D function.

Parameters	Fitting results	Parameters	Fitting results
Z_0	0.4571	B_1	3.8210
A_1	0.0393	B_2	-12.2976
A_2	-0.1059	B_3	9.5222
A_3	0.0212	B_4	-2.2712
A_4	-0.0013	B_5	2.5426

4.3. Fractal-Based SWCC Model in Terms of Capillary Flow. The pore distribution of the soil satisfies the fractal model. Therefore, the fractal theory has a unique advantage in studying the water-holding capacity of unsaturated soil, which can reduce the empirical parameters in the existing complex SWCC model. As Mandelbrot [60] proposed, the relationship between the cumulative volume $V(\leq r)$ of pores with a pore diameter r less than or equal to r and the fractal dimension D can be expressed as

$$V(\leq r) = Cr^{3-D}, \tag{8}$$

where C is a constant. For determining the form of pore water in unsaturated soil, it is assumed that when the water content is less than the residual water content, the pore water is adsorbed around the soil particles and cannot move freely, which can be regarded as a part of solid particles. Once the pores less than or equal to r are filled with water, the relative volumetric moisture content θ' can be regarded as

$$\theta' = Cr^{3-D}, \tag{9}$$

where θ' is the difference between the volumetric water content θ and the residual volumetric water content θ_r. Similarly, the relative volumetric water content at saturation can be generated by substituting r for $r_{\max}$ in Equation (9),

$$\theta_s' = Cr_{\max}^{3-D}, \tag{10}$$

where θ_s' is equal to the volumetric water content at saturation θ_s minus the volumetric water content at residual θ_r. Combined with the Young-Laplace theory, the fractal-based SWCC model in terms of capillary flow can be obtained

$$\theta' = \theta_s'\left(\frac{\psi_e}{\psi}\right)^{3-D}. \tag{11}$$

The intercept p and slope k of the straight line of $\ln(\theta - \theta_r)$ and $-\ln\psi$ can be used to determine the fractal dimension D and ψ_e (air entry value or air expulsion value), that is

$$\ln(\theta - \theta_r) = \ln(\theta_s - \theta_r) + (3 - D)\ln\psi_e - (3 - D)\ln\psi. \tag{12}$$

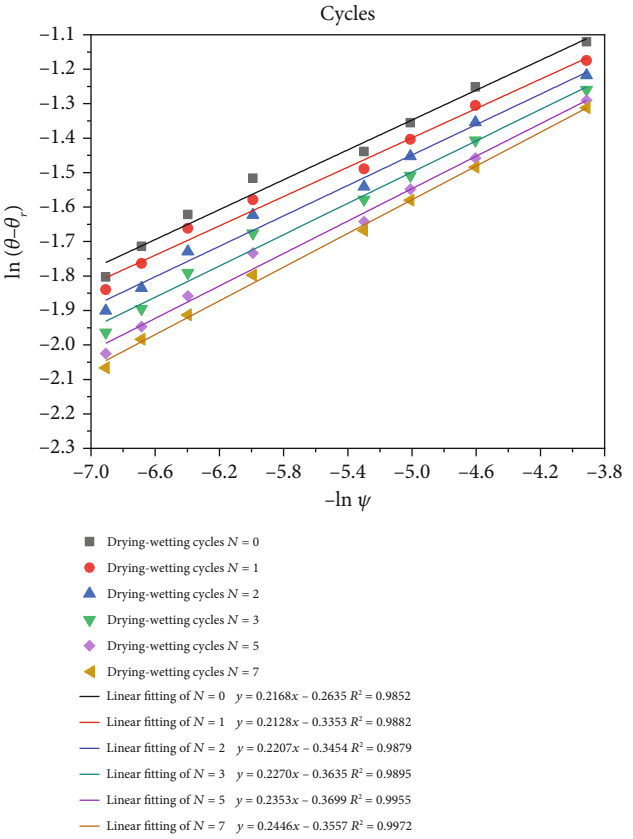

Figure 12: Fitting results of $\ln(\theta - \theta_r)$ against $-\ln\psi$ for residual soil.

The residual volumetric water content θ_r can be obtained by the four-parameter VG model (Table 4). When the value of the residual volumetric water content rate is ignored, the fractal-based SWCC model considering capillary flow can be transformed into the same equation reported by Jin et al. [26] and Xu [61]. Obviously, the SWCC with a matric suction range of ψ_e to ψ_r is affected by capillary force, which is associated with micro-pore structure of soils and its POSD curve follows the geometric fractal theory. As can be seen from the fitting results in Figure 12, the linear correlation coefficient between $\ln(\theta - \theta_r)$ and $-\ln\psi$ is above 0.9882, and the fractal dimensions are all between 2 and 3, indicating that the fractal-based SWCC model clearly describes the residual soil water retention performance under different numbers of drying–wetting cycles and consistent with the fractal theoretical value. Furthermore, it can be seen that the fractal dimension D gradually decreases with the increase in the number of drying–wetting cycles. However, the magnitude of the decrease is small, so the average fractal dimension D in the entire drying–wetting period can be regarded as a constant, which can be taken as 2.7735 (Table 7). At the same time, it is also noted that the air expulsion value determined by the VG and fractal-based SWCC models are different; the value obtained by the former is larger than that of the latter, which is mainly because the air expulsion value decreases significantly with the increase in the number of macro-pores caused by the drying–wetting cycles.

Table 7: Determination of the values of fractal dimension of drying–wetting cycle samples.

Drying–wetting cycles N	$k = 3 - D$	p	D	R^2	The mean value of D
0	0.2168	-0.2635	2.7832	0.9852	2.7735
1	0.2128	-0.3353	2.7872	0.9882	
2	0.2207	-0.3454	2.7793	0.9879	
3	0.2270	-0.3635	2.7730	0.9895	
5	0.2353	-0.370	2.7647	0.9955	
7	0.2466	-0.3557	2.7534	0.9972	

Notably, the above formula is only applicable to the estimation of water content in the capillary flow. When the soil is in dry or high suction condition, the water in the soil exists in the form of membrane water and suction water. The pore water in the absorbed film segment is influenced by the solid–liquid interaction mechanism, while the pore water in the tightly absorbed segment is maintained by the molecular bond mechanism. The POSD curve of residual soil obtained via the NMR test shows that the soil has a double-porous structure; however, the SWCC obtained using the pressure plate test cannot effectively and comprehensively reflect the water-holding performance of the double-pore structure. Therefore, it is necessary to measure the water content of undisturbed residual soil in different high suction ranges by combining the filter paper method and saturated salt solution vapor balance method to achieve the goal of deeply revealing the fractal model for SWCC and the evolution law of POSD of residual soil over the entire range of matric suction under drying–wetting cycles.

5. Conclusions

(1) The water-holding capacity of residual soil decreases with an increase in the number of drying–wetting cycles and gradually becomes stable after five cycles. The four-parameter VG model has proved to be strongly applicable to the prediction of SWCC of undisturbed residual soil under different numbers of drying–wetting cycles

The T_2 spectral distribution curve of the residual soil presents an obvious bimodal pattern, in which the main peak reflects the micro-pores between particles in the soil aggregates, and the secondary peak represents the macro-pores between aggregates. With an increase in the number of drying–wetting cycles, not only the peaks gradually increased and shifted to the right but also the T_2 spectral area and porosity of the residual soil, bright area in the MRIs, and water signal of the soil sample gradually increased. These results indicate that the internal double-pore structure continues to evolve in number and size. An increase in the number of drying–wetting cycles decreases the proportions of micro-pores and small pores in the soil and increases the proportions of meso-pores and macro-pores. Overall, the number of drying–wetting cycles has a greater effect on the small pores and macro-pores than on the micro-pores and meso-pores

The POSD curve of the soil is related to the SWCC. Theoretically, the product of the matric suction ψ and relaxation time T_2 should be constant at a constant temperature, but the measured data show that ψT_2 fluctuates considerably. A modified VG model based on the cumulative pore volume is proposed that can well reflect the POSD of soil subjected to drying–wetting cycles. Then, a Rational2D surface equation, which can comprehensively reflect the internal relationship between the number of drying–wetting cycles N, SWCC parameters (α, n, m) and POSD curve parameters (a, b, c), is constructed to predict the change in the water-holding capacity of residual soil

(2) The fractal-based SWCC model based on capillary flow proves that the matric suction has a good linear correlation with the relative volumetric water content in the log-log scale. Although the fractal dimension decreases with the increase of the number of drying–wetting cycles, the magnitude of the decrease is limited, and it can be regarded as a constant during the entire drying–wetting cycle

Data Availability

The data used to support the findings of this study are available from the corresponding author upon request.

Conflicts of Interest

The authors declare that they have no conflicts of interest.

Acknowledgments

This work was supported by the National Nature Science Foundation of China (grant numbers 41702288 and 41861134011), the Outstanding Youth Fund Project of Fujian Agriculture and Forestry University, China (grant number XJQ202014), and the Natural Science Foundation of Fujian Province, China (grant number 2022J01157).

References

[1] H. Rahardjo, A. Satyanaga, E. C. Leong, Y. S. Ng, and H. T. C. Pang, "Variability of residual soil properties," *Engineering Geology*, vol. 141, pp. 124–140, 2012.

[2] G. S. Guan, H. Rahardjo, and L. E. Choon, "Shear strength equations for unsaturated soil under drying and wetting," *Journal of Geotechnical and Geoenvironmental Engineering*, vol. 136, no. 4, pp. 594–606, 2010.

[3] S. H. Md, K. Ling-wei, and Y. Song, "Effect of drying-wetting cycles on saturated shear strength of undisturbed residual soils," *American Journal of Civil Engineering*, vol. 4, no. 4, pp. 143–150, 2016.

[4] D. Gallipoli, A. Gens, R. Sharma, and J. Vaunat, "An elasto-plastic model for unsaturated soil incorporating the effects of suction and degree of saturation on mechanical behaviour," *Géotechnique*, vol. 53, no. 1, pp. 123–135, 2003.

[5] E. C. Leong and H. Rahardjo, "Permeability functions for unsaturated soils," *Journal of Geotechnical and Geoenvironmental Engineering*, vol. 123, no. 12, pp. 1118–1126, 1997.

[6] S. K. Vanapalli, D. G. Fredlund, D. E. Pufahl, and A. W. Clifton, "Model for the prediction of shear strength with respect to soil suction," *Canadian Geotechnical Journal*, vol. 33, no. 3, pp. 379–392, 1996.

[7] F. Chu, S. J. Shao, and C. L. Chen, "Experimental research on influences of dry density and vertical stress on soil-water characteristic curves of intact unsaturated loess," *Chinese Journal of Rock Mechanics and Engineering*, vol. 33, no. 2, pp. 413–420, 2014.

[8] W. J. Rawls, T. J. Gish, and D. L. Brakensiek, "Estimating soil water retention from soil physical properties and characteristics," *Advances in Soil Science*, vol. 16, pp. 213–234, 1991.

[9] R. D. Williams, L. R. Ahuja, and J. W. Naney, "Comparison of methods to estimate soil water characteristics from soil texture, bulk density, and limited data," *Soil Science*, vol. 153, no. 3, pp. 172–184, 1992.

[10] R. D. Alves, G. de FN Gitirana Jr., and S. K. Vanapalli, "Advances in the modeling of the soil-water characteristic curve using pore- scale analysis," *Computers and Geotechnics*, vol. 127, article 103766, 2020.

[11] L. M. Arya and J. F. Paris, "A physicoempirical model to predict the soil moisture characteristic from particle-size distribution and bulk density data," *Soil Science Society of America Journal*, vol. 45, no. 6, pp. 1023–1030, 1981.

[12] J. Chai and P. Khaimook, "Prediction of soil-water characteristic curves using basic soil properties," *Transportation Geotechnics*, vol. 22, article 100295, 2020.

[13] Y. Li and S. K. Vanapalli, "A novel modeling method for the bimodal soil-water characteristic curve," *Computers and Geotechnics*, vol. 138, article 104318, 2021.

[14] Q. Zhai, H. Rahardjo, A. Satyanaga, and G. Dai, "Estimation of the soil-water characteristic curve from the grain size distribution of coarse-grained soils," *Engineering Geology*, vol. 267, article 105502, 2020.

[15] R. H. Brooks and A. T. Corey, "Hydraulic properties of porous media and their relation to drainage design," *Transactions of the ASAE*, vol. 7, no. 1, pp. 26–28, 1964.

[16] W. R. Gardner, "Some steady-state solutions of the unsaturated moisture flow equation with application to evaporation from a water table," *Soil Science*, vol. 85, no. 4, pp. 228–232, 1958.

[17] M. T. Van Genuchten, "A closed-form equation for predicting the hydraulic conductivity of unsaturated soils," *Soil Science Society of America Journal*, vol. 44, no. 5, pp. 892–898, 1980.

[18] D. G. Fredlund, A. Xing, and S. Huang, "Predicting the permeability function for unsaturated soils using the soil-water characteristic curve," *Canadian Geotechnical Journal*, vol. 31, no. 4, pp. 533–546, 1994.

[19] X. Li, J. H. Li, and L. M. Zhang, "Predicting bimodal soil-water characteristic curves and permeability functions using physically based parameters," *Computers and Geotechnics*, vol. 57, pp. 85–96, 2014.

[20] M. D. Fredlund, D. G. Fredlund, and G. W. Wilson, "An equation to represent grain-size distribution," *Canadian Geotechnical Journal*, vol. 37, no. 4, pp. 817–827, 2000.

[21] A. Satyanaga, H. Rahardjo, E. C. Leong, and J. Y. Wang, "Water characteristic curve of soil with bimodal grain-size distribution," *Computers and Geotechnics*, vol. 48, pp. 51–61, 2013.

[22] M. A. A. Soto, H. K. Chang, and M. T. Van Genuchten, "Fractal-based models for the unsaturated soil hydraulic functions," *Geoderma*, vol. 306, pp. 144–151, 2017.

[23] G. Tao, Y. Chen, L. Kong, H. Xiao, Q. Chen, and Y. Xia, "A simple fractal-based model for soil-water characteristic curves incorporating effects of initial void ratios," *Energies*, vol. 11, no. 6, article 1419, 2018.

[24] M. Soldi, L. Guarracino, and D. Jougnot, "A simple hysteretic constitutive model for unsaturated flow," *Transport in Porous Media*, vol. 120, no. 2, pp. 271–285, 2017.

[25] H. Tao, C. Chen, P. Jiang, and L. Tang, "Soil water characteristic curves based on particle analysis," *Procedia Engineering*, vol. 174, pp. 1289–1295, 2017.

[26] T. Jin, X. Cai, Y. Chen, S. Jiang, and W. Wei, "A fractal-based model for soil water characteristic curve over entire range of water content," *Capillarity*, vol. 2, no. 4, pp. 66–75, 2019.

[27] G. Bodner, P. Scholl, and H. P. Kaul, "Field quantification of wetting-drying cycles to predict temporal changes of soil pore size distribution," *Soil and Tillage Research*, vol. 133, pp. 1–9, 2013.

[28] F. J. Leij, T. A. Ghezzehei, and D. Or, "Modeling the dynamics of the soil pore-size distribution," *Soil and Tillage Research*, vol. 64, no. 1-2, pp. 61–78, 2002.

[29] X. T. Xu and W. B. Jian, "Research on SWCC of unsaturated natural residual soil," *Journal of Engineering Geology*, vol. 23, no. 4, pp. 668–674, 2015.

[30] X. T. Xu, W. B. Jian, and N. S. Wu, "Influence of repeated wetting cycles on shear properties of natural residual soil," *China Journal of Highway and Transport*, vol. 30, no. 2, pp. 33–40, 2017.

[31] R. An, L. Kong, X. Zhang, and C. Li, "Effects of dry-wet cycles on three-dimensional pore structure and permeability characteristics of granite residual soil using X-ray micro computed tomography," *Journal of Rock Mechanics and Geotechnical Engineering*, vol. 14, no. 3, pp. 851–860, 2022.

[32] R. P. Chapuis, "Analyzing grain size distributions with the modal decomposition method: literature review and procedures," *Bulletin of Engineering Geology and the Environment*, vol. 80, no. 9, pp. 6649–6666, 2021.

[33] T. Wen, L. Shao, X. Guo, and Y. Zhao, "Experimental investigations of the soil water retention curve under multiple drying–wetting cycles," *Acta Geotechnica*, vol. 15, no. 11, pp. 3321–3326, 2020.

[34] L. W. Kong, H. M. Sayem, and H. Tian, "Influence of drying-wetting cycles on soil-water characteristic curve of undisturbed granite residual soils and microstructure mechanism by nuclear magnetic resonance (NMR) spin-spin relaxation time (T2) relaxometry," *Canadian Geotechnical Journal*, vol. 55, no. 2, pp. 208–216, 2018.

[35] L. F. Pires, A. C. Auler, W. L. Roque, and S. J. Mooney, "X-ray microtomography analysis of soil pore structure dynamics under wetting and drying cycles," *Geoderma*, vol. 362, article 114103, 2020.

[36] M. Wang, G. N. Pande, L. W. Kong, and Y. T. Feng, "Comparison of pore-size distribution of soils obtained by different methods," *International Journal of Geomechanics*, vol. 17, no. 1, article 06016012, 2017.

[37] S. Costabel and U. Yaramanci, "Estimation of water retention parameters from nuclear magnetic resonance relaxation time distributions," *Water Resources Research*, vol. 49, no. 4, pp. 2068–2079, 2013.

[38] F. Jaeger, S. Bowe, H. Van As et al., "Evaluation of 1H NMR relaxometry for the assessment of pore-size distribution in soil samples," *European Journal of Soil Science*, vol. 60, no. 6, pp. 1052–1064, 2009.

[39] H. Tian, C. F. Wei, H. Z. Wei, R. Yan, and P. Chen, "An NMR-based analysis of soil–water characteristics," *Applied Magnetic Resonance*, vol. 45, no. 1, pp. 49–61, 2014.

[40] Y. R. Zhao, X. H. Sun, T. D. Wen, R. Chen, and L. Huang, "Micro-structural evolution of granite residual soil under external loading based on X-ray micro-computed tomography," *KSCE Journal of Civil Engineering*, vol. 25, no. 8, pp. 2836–2846, 2021.

[41] T. T. Ma, C. F. Wei, C. Q. Yao, and P. Yi, "Microstructural evolution of expansive clay during drying–wetting cycle," *Acta Geotechnica*, vol. 15, no. 8, pp. 2355–2366, 2020.

[42] J. R. Zhang, G. Niu, X. C. Li, and D.'. Sun, "Hydro-mechanical behavior of expansive soils with different dry densities over a wide suction range," *Acta Geotechnica*, vol. 15, no. 1, pp. 265–278, 2020.

[43] N. F. Zhao, W. M. Ye, B. Chen, Y. G. Chen, and Y. J. Cui, "Modeling of the swelling–shrinkage behavior of expansive clays during wetting–drying cycles," *Acta Geotechnica*, vol. 14, no. 5, pp. 1325–1335, 2019.

[44] W. M. Albadri, M. J. M. Noor, and I. J. Alhani, "The relationship between the shear strength and water retention curve of unsaturated sand at different hydraulic phases," *Acta Geotechnica*, vol. 16, no. 9, pp. 2821–2835, 2021.

[45] K. Liao, Y. P. Wu, F. S. Miao, L. Li, and Y. Xue, "Time-varying reliability analysis of Majiagou landslide based on weakening of hydro-fluctuation belt under wetting-drying cycles," *Landslides*, vol. 18, no. 1, pp. 267–280, 2021.

[46] H. Miao and G. Wang, "Effects of clay content on the shear behaviors of sliding zone soil originating from muddy interlayers in the Three Gorges Reservoir, China," *China. Engineering Geology*, vol. 294, article 106380, 2021.

[47] Q. Cheng, C. S. Tang, H. Zeng, C. Zhu, N. An, and B. Shi, "Effects of microstructure on desiccation cracking of a compacted soil," *Engineering Geology*, vol. 265, article 105418, 2020.

[48] W. L. Hu, W. C. Cheng, S. J. Wen, and M. Mizanur Rahman, "Effects of chemical contamination on microscale structural characteristics of intact loess and resultant macroscale mechanical properties," *Catena*, vol. 203, article 105361, 2021.

[49] P. Li, W. L. Xie, R. Y. S. Pak, and S. K. Vanapalli, "Microstructural evolution of loess soils from the Loess Plateau of China," *Catena*, vol. 173, pp. 276–288, 2019.

[50] C. W. W. Ng, H. Sadeghi, S. K. B. Hossen, C. F. Chiu, E. E. Alonso, and S. Baghbanrezvan, "Water retention and volumetric characteristics of intact and re-compacted loess," *Canadian Geotechnical Journal*, vol. 53, no. 8, pp. 1258–1269, 2016.

[51] A. Azizi, G. Musso, and C. Jommi, "Effects of repeated hydraulic loads on microstructure and hydraulic behaviour of a compacted clayey silt," *Canadian Geotechnical Journal*, vol. 57, no. 1, pp. 100–114, 2020.

[52] R. Chen and C. W. W. Ng, "Impact of wetting-drying cycles on hydro-mechanical behavior of an unsaturated compacted clay," *Applied Clay Science*, vol. 86, pp. 38–46, 2013.

[53] C. S. Tang, Q. Cheng, T. Leng, B. Shi, H. Zeng, and H. I. Inyang, "Effects of wetting-drying cycles and desiccation cracks on mechanical behavior of an unsaturated soil," *Catena*, vol. 194, article 104721, 2020.

[54] X. T. Xu and W. B. Jian, *Research on the Response and Failure Process of Unsaturated Soil Slope under Rainfall Infiltration*, China Communications Press, Beijing, 2020.

[55] J. Liu, Y. Wu, C. Z. Cai et al., "Investigation into water retention and gas permeability of Opalinus clay," *Environmental Earth Sciences*, vol. 77, no. 5, pp. 1–13, 2018.

[56] X. T. Xu, L. J. Shao, J. B. Huang et al., "Effect of wet-dry cycles on shear strength of residual soil," *Soils and Foundations*, vol. 61, no. 3, pp. 782–797, 2021.

[57] T. L. T. Zhan, R. Chen, and C. W. W. Ng, "Wetting-induced softening behavior of an unsaturated expansive clay," *Landslides*, vol. 11, no. 6, pp. 1051–1061, 2014.

[58] N. F. Zhao, W. M. Ye, Y. G. Chen, B. Chen, and Y. J. Cui, "Investigation on swelling-shrinkage behavior of unsaturated compacted GMZ bentonite on wetting-drying cycles," *Bulletin of Engineering Geology and the Environment*, vol. 78, no. 1, pp. 617–627, 2019.

[59] X. T. Xu, W. B. Jian, N. S. Wu, X. Xu, and L. J. Shao, "Void ratio dependent water retention model for a deformable residual clay," *International Journal of Geomechanics*, vol. 20, no. 8, article 04020131, 2020.

[60] B. B. Mandelbrot, *The Fractal Geometry of Nature*, FREEMAN W H, New York, 1982.

[61] Y. Xu, "Calculation of unsaturated hydraulic conductivity using a fractal model for the pore-size distribution," *Computers and Geotechnics*, vol. 31, no. 7, pp. 549–557, 2004.